Batteries Hot Paper

How to cite: *Angew. Chem. Int. Ed.* **2022**, *61*, e202113315
International Edition: doi.org/10.1002/anie.202113315
German Edition: doi.org/10.1002/ange.202113315

Anthraquinone Covalent Organic Framework Hollow Tubes as Binder Microadditives in Li–S Batteries

Can Guo[+], Ming Liu[+], Guang-Kuo Gao[+], Xi Tian, Jie Zhou, Long-Zhang Dong, Qi Li, Yifa Chen, Shun-Li Li, and Ya-Qian Lan**

Abstract: *The exploration of new application forms of covalent organic frameworks (COFs) in Li–S batteries that can overcome drawbacks like low conductivity or high loading when typically applied as sulfur host materials (mostly ≈20 to ≈40 wt% loading in cathode) is desirable to maximize their low-density advantage to obtain lightweight, portable, or high-energy-density devices. Here, we establish that COFs could have implications as microadditives of binders (≈1 wt% in cathode), and a series of anthraquinone-COF based hollow tubes have been prepared as model microadditives. The microadditives can strengthen the basic properties of the binder and spontaneously immobilize and catalytically convert lithium polysulfides, as proved by density functional calculations, thus showing almost doubly enhanced reversible capacity compared with that of the bare electrode.*

Introduction

Lithium–sulfur (Li–S) batteries are promising candidates for future rechargeable battery systems, owing to the ultra-high theoretical energy density (2600 Wh kg^{-1}), superior theoretical specific capacity (1675 mAh g^{-1}) and the conspicuous advantages of sulfur (e.g., low cost, environmental friendliness and natural abundance).[1] Nonetheless, the inherent obstacles of Li–S batteries, such as large volumetric variation (≈80%), shuttling effect of soluble lithium polysulfides (LiPSs), the poor electrical conductivity of sulfur, and corrosion of lithium metal anode, would cause structural instability and shorten the cycle lifespan, which largely dampen their potentials in practical applications.[2] Extensive efforts have been reported like accommodation of volume changes with porous structures, suppressing LiPSs migration with adsorbents, enhancing the conversion of LiPSs with catalysts, or facilitating electron/ion transferring with conductors, in which the multiple requirements would generally enhance the difficulty in material design and are hard to be satisfied with techniques in one aspect.[3] Besides, these traditional attempts are still at their early stages, and innovative attempts that can change the typical application forms with boosted performances would be much essential, especially for the development of highly desired light-weight or portable Li–S batteries.[4]

Binder, as one of the key components of Li–S batteries applied as early as 1980s, has garnered much attention recently in the battery community.[5] Binders are designed to provide strong adhesion with active materials, conductive additives and current collector, and a strong skeleton to accommodate the stress–strain during the electrochemical process, which typically occupy a small portion of the entire battery (weight, <10 wt% and cost, <2%) and might be neglected.[6] In general, binders can be mainly divided into natural (e.g., sodium alginate (SA), sodium carboxymethylcellulose (CMC)) and artificial (e.g., poly(ethylene oxide) (PEO), and poly(vinylidene difluoride) (PVDF), polyvinyl pyrrolidone (PVP), poly(acrylic acid) (PAA)) ones.[6b,7] During past decades, the functions of binders have been explored and shifted from simple mechanical stabilizers to electrochemical regulators (e.g., immobilization of LiPSs or electron/ion transporter) as driven by a deeper understanding of multiphase conversion chemistry in Li–S battery system.[6b,7a,8] Nowadays, PVDF as a kind of artificial binders has reported to be the dominant one due to its mechanical, chemical and electrochemical stability benefits yet is still restricted by the drawbacks like the lack of strong interactions with electroactive materials, insufficient mechanical properties, low electronic and lithium-ion conductivities and inability to adapt volume expansion during cycling process, which is inadequate to fulfill the demands of batteries with high energy density and remains a commonly existed bottleneck for single polymer binder.[12] Function modification, integration with other binders, or introduction of additives would be promising strategies to permit binders with higher properties for Li–S batteries.[9] Among them, binder additives especially in micro-amount, may be a more alternative method to solve the issues of Li–S batteries compared with other strategies when taking the ease of processing, energy consumption, and requirement

[*] Dr. C. Guo,[+] G.-K. Gao,[+] J. Zhou, Prof. Y. Chen, Prof. Y.-Q. Lan
School of Chemistry, National and Local Joint Engineering Research Center of MPTES in High Energy and Safety LIBs, Engineering Research Center of MTEES (Ministry of Education), and Key Lab. of ETESPG(GHEI), South China Normal University
Guangzhou 510006 (P. R. China)
E-mail: chyf927821@163.com
yqlan@njnu.edu.cn
yqlan@m.scnu.edu.cn

Dr. M. Liu,[+] X. Tian, L.-Z. Dong, Q. Li, Prof. Y. Chen, Prof. S.-L. Li
Jiangsu Collaborative Innovation Centre of Biomedical Functional Materials, Jiangsu Key Laboratory of New Power Batteries, School of Chemistry and Materials Science, Nanjing Normal University
Nanjing 210023 (P. R. China)
Homepage: https://www.yqlangroup.com/

[+] These authors contributed equally to this work.

Supporting information (including 47 figures and five tables) and the ORCID identification number(s) for the author(s) of this article can be found under: https://doi.org/10.1002/anie.202113315.

of light-weight/portable battery devices into consideration. Nonetheless, the research on additives of binders is still in its infancy, and there are several immature while much-preferred areas like the construction of porous structures in binders to alleviate the sulfur volume expansion, the investigation of binders as electrocatalysts for the LiPSs conversion, or the tuning of electrolyte wetting ability for binders to facilitate electron/ion diffusion, etc.[8] Therefore, it is necessary to explore techniques like microadditive methods for binders without changing the existing technical conditions while boosting performance to meet the light-weight/portable demand of Li–S batteries in high energy-density electronics or electric vehicles.

With these considerations, covalent organic frameworks (COFs), a kind of porous organic polymers composed of light-weight elements with high porosity and tunable functionality, come to our mind as a prototype for designing efficient microadditives of binders.[10] COFs have attracted considerable attention in Li–S batteries and are generally investigated as the host materials of sulfur owing to the advantages like large specific surface areas, well-aligned pore channels, tunable functionality and precise distribution of active sites that enable high sulfur loadings, inhibition of polysulfide shuttling, alleviation of sulfur volume change, and facilitating ion diffusion, etc.[11] However, the poor conductivity and low density of COFs has largely restricted the applications of COFs as the host materials when taking the relatively high loadings of COFs (mostly ≈20 to ≈40 wt% loading in the cathode) into consideration, in which the almost insulated COFs structures coupling with the low conductivity of sulfur would result in high internal resistance and low special energy density.[12] Therefore, we speculate that if it is possible to apply COFs as the microadditives of binders for Li–S batteries, providing the following advantages: 1) COFs in low density (the density can be as low as ≈0.1 g cm^{-3})[13] can nicely fit the light-weight principle when applied as the microadditives of binders to obtain low-cost and portable Li–S batteries;[14] 2) the pore channels of COFs can not only promote electrolyte wetting but also facilitate the ion transportation;[15] 3) the functional groups like anthraquinone, diazole, imine-based, imidazolium keto-carbonyl and azo groups, accessible by modification of COFs structures, would contribute to the immobilization or even catalytic conversion of LiPSs;[6a] 4) the electronegative polar groups (e.g., -OH, -F, and heteroatom, etc.) in selected ligands of COFs can improve the mechanical strength of binders and enhance the adhesion among the sulfur, conductive additives and current collector;[6a,16] 5) COFs in various morphologies like hollow tubes or hollow spheres would be favorable for the accommodation of volume change during charge-discharge process.[11b,17] Besides, well-defined crystalline structures of COFs could provide excellent platforms for investigating the possible mechanisms in Li–S batteries.[16] As far as we know, there are few reports of COFs as microadditives of binders, which might be a start point for the applications of COFs in this area.

Herein, we present the first case of applying COFs as microadditives of binders in Li–S batteries (Figure 1). A series of anthraquinone COF-based hollow tubes

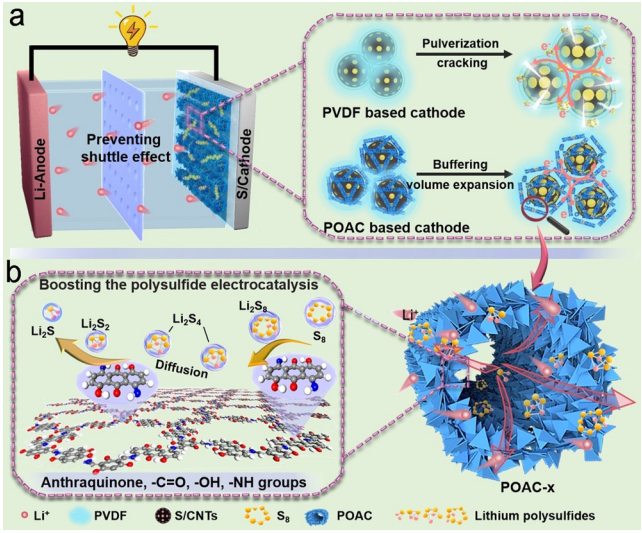

Figure 1. Schematic illustration of POAC-*x* (*x* = 1–5) as microadditives to binders for Li–S batteries.

(PVDF@OH-AAn-COF, denoted as POAC-*x*, *x* = 1–5) have been prepared through the in situ self-assembly of PVDF, 1,5-diamino-4,8-dihydroxyanthraquinone (OH-AAn) and 1,3,5-triformylphloroglucinol (TP) and applied as the microadditives of binders (0.5–4.0 wt% in cathode). Introduced POAC-*x* (*x* = 1–5) can obviously strengthen the properties (e.g., viscosity, electrolyte wetting and Li^+ transportation) of binder and enable to repair the mechanical damage and cracks in the electrode spontaneously during cycling, which results in more stable mechanical and electrical connections among the active materials than traditional sulfur cathode (Figure 1a). Specifically, the electrode with POAC-4 as microadditive (1.0 wt% in the cathode) presents almost doubly enhanced reversible capacity (initial specific capacity of 1292.5 mAh g^{-1}, 805.5 mAh g^{-1} over 300 cycles at 0.5 C) than that of PVDF-based electrode and exhibits ≈99.9% Coulombic-efficiency (CE). In addition, POAC-4 based electrode shows an impressively high capacity of 517.0 mAh g^{-1} after 600 cycles at 2 C, which is almost twice than that of bare electrode. Notably, the achieved performances are superior to most of reported COF-based or binder-based Li–S batteries. In addition, density functional theory (DFT) calculations demonstrate that anthraquinone-COF hollow tubes possess high affinity and catalysis ability for LiPSs (Figure 1b), which will play a critical role in maintaining high electrochemical performance.

Results and Discussion

The samples are prepared by in situ self-assembly of PVDF, TP and OH-AAn, during which OH-AAn-COF is formed through a Schiff base reaction, and PVDF is encapsulated at the same time (detail see Methods) (Figure S1). In this process, the loading of PVDF can be adjusted with different addition amounts in the precursors to produce the corresponding products of POAC-*x* (*x* = 1–5). The powder X-ray diffraction (PXRD) tests confirm that the patterns of

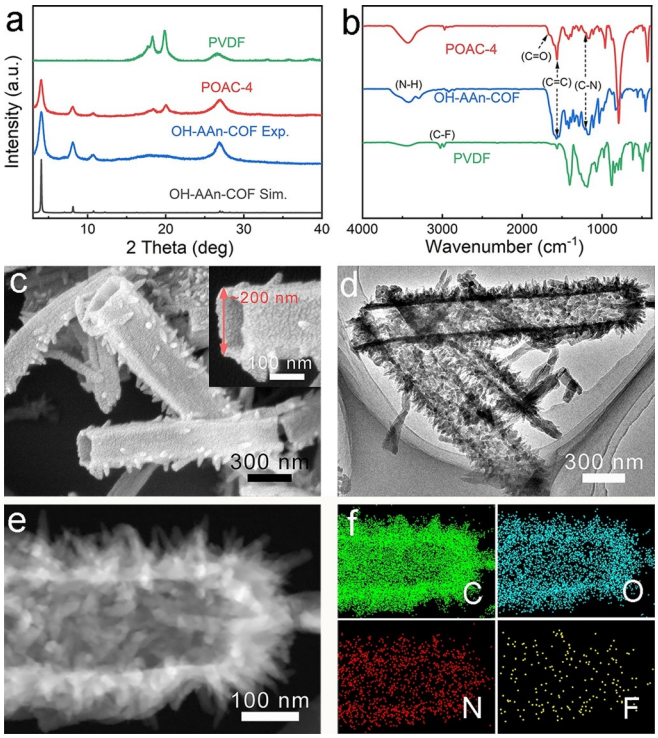

Figure 2. PXRD, FT-IR and morphology characterizations of POAC-4. a) PXRD patterns of POAC-4, OH-AAn-COF and PVDF. b) FT-IR spectra of POAC-4, OH-AAn-COF and PVDF. c) SEM image of POAC-4. d) TEM image of POAC-4. e, f) Elemental mapping images of POAC-4.

POAC-x ($x = 1$–5) are the integrated patterns of PVDF and OH-AAn-COF, showing the coexistence of them in POAC-x ($x = 1$–5) (Figure 2a and Figure S2). Taking POAC-4 for example, the peaks at 4.1°, 8.1°, 10.8°, 13.7° and 27.3° are assigned to (1 0 0), (2 0 0), (3 1 0), (3 0 0) and (0 0 1) crystal facets of OH-AAn-COF, respectively, while the additional PXRD peaks appeared at 18.3°, 20.3° are ascribed to that of PVDF (Figure 2a).[18] From POAC-1 to POAC-5, the peaks of PVDF gradually become stronger with the enhanced addition of PVDF in the precursors, implying the increased loading of PVDF (Figure S2). Besides, the components of POAC-x ($x = 1$–5) have been further evaluated by Fourier-transform infrared spectroscopy (FT-IR) measurements. Taking POAC-4 as an example, the disappearance of characteristic peaks of imine (C=N) groups where the enol form can be converted to the keto form, implies the successful formation of OH-AAn-COF in POAC-4 (Figure 2b and Figure S3). The strong peaks corresponding to C=C ($\approx 1564\ cm^{-1}$) and C-N ($\approx 1265\ cm^{-1}$) stretching bands (assigning to ketoenamine form) are similar with the peaks of OH-AAn-COF.[18b] In addition, the C-F stretching appeared at $1176\ cm^{-1}$ confirms the successful encapsulation of PVDF in POAC-4 compared with that of PVDF (Figure 2b). Similarly, the FT-IR spectra of POAC-1, POAC-2, POAC-3 and POAC-5 are closed to that of POAC-4, supporting the coexistence of PVDF and OH-AAn-COF in these hybrid materials (Figure S4).

To investigate the chemical bonding nature of C, O, F and N atoms and quantitative elemental analysis of the samples, X-ray photoelectron spectroscopy (XPS) measurements have been conducted. For the XPS spectra of POAC-x ($x = 1$–5), four main peaks with binding energies of 284.6, 411.1, 546.1 and 699.1 eV are ascribed to C 1 s, N 1 s, O 1 s and F 1 s, respectively (Figure S5). Taking POAC-4 for instance, the C 1 s spectra exhibit the main peak at 290.7 eV, which can be assigned to the C-F bond of PVDF (Figure S6a). Besides, peaks appearing at 284.6, 286.1, 288.1, and 289.6 eV can be featured in C-O/C-N, C=O/quinone-type carbon, C=C and π–π* transition, respectively.[19] For O 1 s scan spectra, it can be deconvoluted into three peaks at 531.1, 532.8 and 535.8 eV, ascribing to O = C/quinone-type oxygen, O-C, O-H groups, respectively (Figure S6b).[19b] The N 1 s spectrum of POAC-4 reveals a single peak at 399.7 eV, corresponding to the β-ketoenamine nitrogen of OH-AAn-COF (Figure S6c). The first peak at 402.4 eV is observed and fitted into the minor amount of oxidized N species (N-O).[19] Similarly, the C-F bond in POAC-4 is verified by the presence of F 1 s (687.7 eV) (Figure S6d).[20] Similar results can also be detected for POAC-x ($x = 1$, 2, 3 and 5), indicating the coexistence of PVDF and OH-AAn-COF for all of them (Figures S7–S10). Furthermore, the mass percentages of elements for POAC-x ($x = 1$–5) are calculated and listed in Table S1 based on the XPS tests. The results show that the loadings of PVDF in POAC-x ($x = 1$–5) are among the range from 16 to 57 wt%.

To characterize the morphology of the samples, scanning electron microscopy (SEM) and transmission electron microscopy (TEM) tests have been performed. Taking POAC-4 for instance, the SEM test shows a kind of regular hollow tube morphology (length, ≈3 μm; wall thickness, ≈25 nm and outer diameter, ≈200 nm) with a hairy surface (Figure 2c,d). The morphology is further supported by the TEM test, which is similar to that of OH-AAn-COF (Figure S11). Moreover, POAC-x ($x = 1, 2, 3$ and 5) all display hollow tube morphology as proved by the SEM and TEM tests (Figure S12). Among POAC-x ($x = 1$–5), POAC-4 shows the most regular hollow tube morphology when compared with other samples, which might be attributed to the tuning effect of different amounts of PVDF during the formation process. Energy-dispersive X-ray spectroscopy (EDS) mapping images reveal that C, N, O and F are uniformly distributed in POAC-4 (Figure 2f). POAC-x ($x = 1$, 2, 3 and 5) all display similar results in the EDS mapping tests, indicating the uniform distribution of PVDF in these samples (Figure S13).

POAC-x ($x = 1$–5) are a kind of porous hybrid materials assembled from OH-AAn-COF and PVDF, which might inherit the high porosity of OH-AAn-COF. To verify it, N_2 sorption tests have been carried out. Based on the N_2 sorption isotherms at 77 K, the Brunauer-Emmett-Teller surface area (S_{BET}) and pore volume (V_t) of POAC-x ($x = 1$–5) are all lower than that of OH-AAn-COF (S_{BET}, $459\ m^2\,g^{-1}$ and V_t, $0.45\ cm^3\,g^{-1}$) and follow a decreased trend with the increased loading of PVDF (Figure S14a and Table S2). For example, POAC-1 has an S_{BET} of $379\ m^2\,g^{-1}$ and V_t of $0.34\ cm^3\,g^{-1}$, while POAC-5 with higher PVDF loading possesses a lower S_{BET} ($131\ m^2\,g^{-1}$) and V_t ($0.11\ cm^3\,g^{-1}$). Besides, the pore size distribution in the micro-pore range (< 2 nm) follows a decreased trend with the increase of PVDF loading (Figure S14b and Table S2). Taking POAC-1 as an example,

quenched solid-state density functional theory (QSDFT) calculation reveals that its pore size distribution centers at 1.29 nm, while the pore size distribution of POAC-5 decreases to 1.02 nm, which are lower than that of OH-AAn-COF (1.31 nm).[18b] These results demonstrate that the encapsulated PVDF in the pore channels might partially narrow down the pore size, thus resulting in gradually reduced pore size from POAC-1 to POAC-5. The encapsulated PVDF in the pore channels of OH-AAn-COF achieved through the in situ self-assembly of PVDF and COF precursors might aid in enhancing the compatibility of OH-AAn-COF with traditional binders like PVDF, thus strengthening the binder properties. Moreover, the high porosity might impart POAC-x ($x=1$–5) with low density. As a proof-of-concept, the tap densities of OH-AAn-COF and POAC-4 are tested to be as low as 0.07 and 0.20 g cm^{-3}, respectively. The high porosity coupled with low density would permit these hybrid materials with highly accessible surface areas, making them the desired alternatives of microadditives.

The rheological behavior is investigated using a cone-plate rheometer to determine the effect of microadditives on electrochemical performances. The measured viscosity at different shear rates from the steady-state flow-step test clearly shows that all the three slurries (i.e., POAC-4, PVDF and physical mixture (stands for the physical mixture of PVDF and OH-AAn-COF, the mass ratio complies with that of POAC-4)) display a shear thickening thixotropic behavior (Figure 3a).[21] In detail, the viscosities at a shear rate of 1 s^{-1} for POAC-4, physical mixture, and PVDF based slurries are 4.3, 27.3, and 308.7 Pa, respectively, which might be ascribed to the reversible and dynamic networks generated from the interaction between POAC-4 and Super P that leads to associative thickening effect.[22] In POAC-4, the existence of a large number of oxygen-containing groups (e.g., hydroxyl, anthraquinone and keto-carbonyl groups) in OH-AAn-COF coupled with the encapsulated PVDF could forge strong interaction with Super P, as proved by the higher viscosity of POAC-4 than that of the physical mixture.[21] In addition, oscillatory rheological measurements are carried out to further characterize the viscoelastic effect in a stress sweep step test. The variation curves of the "storage modulus" G' (elastic component) and "loss modulus" G'' (viscous component) for POAC-4, physical mixture and PVDF as a function of shear stress are presented and divided into two regions (Figure 3b and Figure S15).[23] In Region I, the value of G' of POAC-4 is higher than G″, which indicates that the POAC-4 and Super P can form network architecture with an elastic-dominant behavior. It exhibits a more liquid-like behavior as the shear stress increases.[22–24] After the G′-G″ crossover point, Region II starts and the G″ becomes higher than G′ with increasing shear stress, indicating a liquid-dominant behavior.[21,22] To evaluate the possibility of the samples as the microadditives of binders, the adhesion tests have been examined, during which the sample is fabricated into a slurry with Super P in N-methyl pyrrolidone solvent (NMP) (90 wt % solutions) (Figure S16). Taking POAC-4 for example, the result shows that the viscosity of POAC-4 displays higher adhesion force (37.2 cp) than that of PVDF (25.5 cp), suggesting that POAC-4 might act as a kind of microadditives

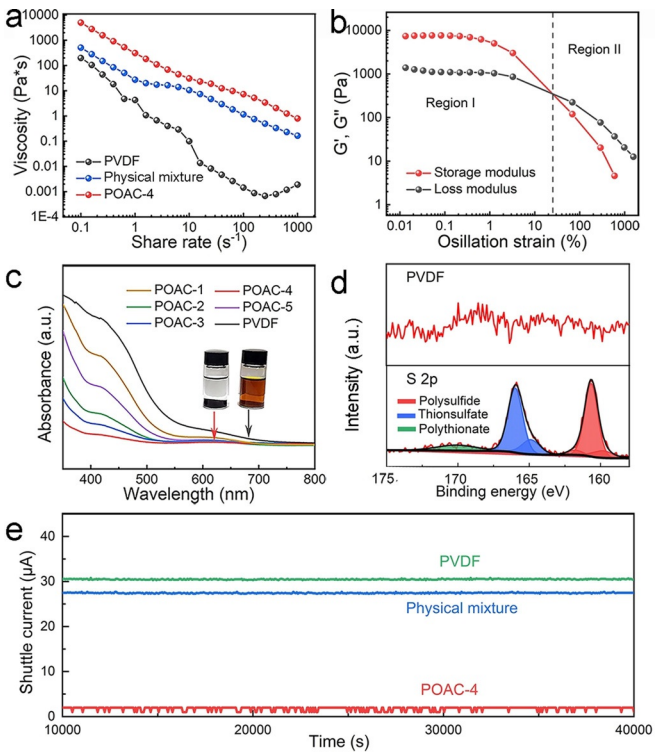

Figure 3. Viscosity, Li_2S_6/shuttling and contact angle tests for POAC-4. a) Viscosity as a function of shear rate for POAC-4, a physical mixture and PVDF. b) Variation of G' and G'' with shear stress for POAC-4. c) Photographs and UV/Vis curves for Li_2S_6 (10 mM) adsorption tests with PVDF and POAC-x ($x=1$–5) in DOL/DME solution; the insert images are POAC-4 (left) and PVDF (right) after adsorption tests. d) S 2p XPS profiles of PVDF and POAC-4 after Li_2S_6 adsorption tests. e) Shuttle current curves for POAC-4, physical mixture, and PVDF-based electrodes with potentiostatic charge at 2.35 V.

to enhance the adhesion force of binder like PVDF. Besides, the adhesion of these binders to the electrode material has been supported by folding experiment and no materials peel off from the electrode during the repeated bending and folding operations bended and folded (Figure S17). This appropriate viscosity together with excellent rheological behavior renders POAC-4 to be a promising candidate as the microadditives of binders in Li–S batteries.

Moreover, the Li_2S_6 adsorption ability has been evaluated by the static adsorption tests in 10 mL Li_2S_6 solution (10 mM) and quantitative traced by UV/Vis spectroscopy (Figure 3c). As witnessed in Figure 3c and Figure S18, POAC-x ($x=1$–5) obviously changes the color of the solution from orange to transparent after 6 h while PVDF only enables slight discoloring at the same time, visually indicating the strong adsorption ability of these hybrid materials. Besides, the UV/Vis adsorption spectra of the corresponding solution for PVDF show a strong peak at ≈420 nm after 6 h, which is attributed to the vibration of Li_2S_6.[25] Notably, the intensity of the Li_2S_6 peak for the solution treated by POAC-x ($x=1$–5) drastically decreases after 6 h (Figure 3c). Especially for POAC-4, the peak at ≈420 nm almost disappears after 6 h. These results prove the high Li_2S_6 adsorption ability, which might be attributed to the strong interactions between Li_2S_6

and the polar functional groups (e.g., anthraquinone, keto-carbonyl and hydroxyl groups) of hybrid materials.[6a] In addition, XPS tests have been performed to study the possible interactions between the samples and LiPSs after Li_2S_6 adsorption for 6 h (Figure 3d). As shown in Figure 3d, the S 2p spectrum of POAC-4 after 6 h test shows the coexistence of thiosulfate, polythionate, and LiPSs. The formation of thiosulfate ($S_2O_3^{2-}$) could be ascribed to reactions between POAC-4 and LiPSs.[25] Besides, The intermediate polythionate [O_3S_2-$(S)_{x-2}$-S_2O_3] indicates the reversible reaction between $S_2O_3^{2-}$ and LiPSs. Correspondingly, there are peaks of C-S^{2-} and C-S at 284.2 and 286.1 eV in the C 1 s spectrum, respectively (Figure S19).[25b,26] Therefore, XPS measurements of POAC-4 before and after Li_2S_6 adsorption verify the strong interaction between POAC-4 and Li_2S_6. In comparison, the complete absence of any S 2p spectrum of PVDF after 6 h test reveals that it has a weak interaction with Li_2S_6 (Figure 3d).

To investigate the suppressing behavior for the "shuttling effect", the samples are assembled into electrodes to test the shuttle currents (Figure 3e). Obviously, the shuttle current of POAC-4 based electrode ($\approx$2.60 μA) is the smallest among all of the examined electrodes, which is only one-tenth and one-twelfth of the physical mixture-based electrode ($\approx$26.02 μA) and PVDF based electrode (31.21 μA), respectively. It reveals that the microadditives can largely enhance the anchoring ability for LiPSs and suppress the shuttling effect in the working cell.[25b] Moreover, contact angle tests have been conducted to evaluate the electrolyte wettability of electrodes with different samples. Introduced POAC-4 can result in decreased contact angle (13.1°) of POAC-4 based electrode when compared with that of PVDF based electrode (20.9°), which might be attributed to the presence of abundant polar groups in POAC-4 that are beneficial for the improvement of wettability (Figure S20).[27]

To verify the electrocatalytic activity of POAC-4 based electrode within a potential window from −0.8 to 0.8 V, symmetric cells are assembled using POAC-4 or bare PVDF based electrodes as both anode and cathode and carried out in cyclic voltammogram (CV) profiles at a scan rate of 50 mV s^{-1} (Figure S21). As a result, the symmetric cells with POAC-4 based electrode exhibit higher current with obvious redox peaks compared to bare PVDF based electrode, implying that POAC-4 possesses better electrochemical kinetics for the rapid redox conversion reactions of LiPSs on the electrolyte/electrode surface (Figure S21).[6a,28] The accelerated redox reaction kinetics of LiPSs might be ascribed to the catalytic activity of POAC-4 in promoting the LiPSs conversion. The kinetics of Li_2S nucleation experiments are tested on POAC-4 and PVDF electrodes surface to prove the catalytic effects (Figure S22). The potentiostatic discharge curves of the aforementioned electrodes are tested at 2.05 V to nucleate Li_2S until the current is lower than 10^{-5} A, in which the capacity of Li_2S conversion of the POAC-4 based electrode is calculated based on the quantity of electric charge according to the Faraday's law.[28,29] Specifically, the capacity of Li_2S precipitation on POAC-4 based electrode (239 mAh g^{-1}) is significantly higher than that of the PVDF based one (173 mAh g^{-1}). Additionally, the POAC-4 based electrode displays a much higher and earlier discharging current peak than that of PVDF-based electrode (Figure S22). These results manifest that the POAC-4 substantially enhances the fast conversion process from LiPSs to Li_2S.

As discussed above, POAC-x (x = 1–5) present a kind of hollow tube morphology with advantages like high porosity, abundant polar functional groups, efficient inhibition of LiPSs shuttling, improvement of wettability and catalytic activity for LiPSs conversion, which would be the desired microadditives of binders in Li−S batteries. To test the properties of Li−S batteries, POAC-x (x = 1–5) as the microadditives are premixed with the binder of PVDF and the mixture acts as the binder (the loadings of POAC-x are controlled to be 0.5, 1.0, 2.0, 3.0 and 4.0 wt % in the cathode) of Li−S battery. S/CNTs, commercial Super P and binder are mixed in NMP solution to produce the slurry and casted onto the surface of Al foil through the doctor blade. Sulfur content of 70.15 wt % is determined via thermal gravimetric analysis (TGA) (Figure S23). The 2032-type coin cell is assembled using a lithium foil as the anode and LiTFSI (1.0 M) in DOL and DME (1:1 by volume) with 1.0 wt % $LiNO_3$ additive as the electrolyte. In the cathode, the contents of POAC-x (x = 1–5) as the microadditives of the binder are among the range from 0.5 to 4.0 wt %. For example, POAC-4 based Li−S cell with the loading of 1.0 wt % is denoted as POAC-4 based Li−S cell (1.0 wt %). In addition, PVDF and physical mixture (stands for physical mixture of PVDF and OH-AAn-COF, the mass ratio complies with that of POAC-4) based cathodes are also prepared as comparisons.

The electrochemical performances of POAC-4 based Li−S cells are tested at different current densities (0.2 C to 2 C, 1 C = 1675 mAh g^{-1}), the performances of the cells with diverse loadings (0.5 to 4.0 wt %) of POAC-4 in the cathode are also measured for comparison. Electrochemical impedance spectroscopy (EIS) measurements for POAC-4 based Li−S cell (0.5 to 4.0 wt %) have been carried out (Figure S24). The Nyquist plots at the open-circuit voltage are composed of a semicircle at both high and medium frequency and an inclined line in the low-frequency region. The high-frequency intercept on the real axis represents the ohmic resistance of the cell, including the electrolyte and electrode resistances. The semicircle at high to medium frequency is attributed to the surface layer and interfacial impedance of the electrodes, and the line belongs to the Li-ion diffusion within the cathodes. The R_{ct} of the cell with 1 wt % POAC-4 in the cathode has a much lower R_{ct} than the cell without microadditive (59 Ω) and other loadings of POAC-4, which implies more effective electric contact and declined charge-transfer resistance within cells (Figures S24 and S25). In order to gain further insight into the effect of POAC-x (x = 1–5) on sulfur cathodes, the R_{ct} of POAC-x (x = 1–5) based cells with 1 wt % microadditive have been tested and POAC-4 is lower than other POAC-x (x = 1, 2, 3, 5) based ones (Figure S26). The EIS results of fresh cells show that the typical Nyquist plots of the POAC-4, physical mixture and PVDF are calculated to be 16 Ω, 29 Ω and 59 Ω, respectively (Figure S25). The decrease of battery resistance results in less internal consumption meanwhile can improve the capacity and safety. There might be a tradeoff between the loading of microadditive and

performances, and it could be explained that excess POAC-4 would cause the poor connection between active material and electrolyte, thus lowering the cell performances. Therefore, we will focus on the Li–S cell with 1.0 wt% POAC-4 to investigate other battery properties.

Obviously, the strong interactions and redox reactions between LiPSs and POAC-4 are the key factors relating to the cycling stability of S electrodes.[25b,26] Figure 4a shows the typical CV curves of the POAC-4 based Li–S cell (1.0 wt%) at a scan rate of 0.1 mV s^{-1} for the first 5 cycles within a voltage window of 1.7 to 2.6 V, where the characteristics for the electrochemical reaction of sulfur with lithium are observed. Two major reduction peaks can be found at around 2.32 and 2.03 V during the cathodic scans, corresponding to the transformation of pristine S (cyclo-S_8 for the initial cycle and Li_2S_8 for the following cycles) to long-chain LiPSs, and the subsequent decomposition of long-chain LiPSs forming final Li_2S_2 and/or Li_2S product, respectively.[29b] During the anodic scan, the CV curves exhibit one intense oxidation peak positioned at around 2.41 V, attributing to the conversion of LiPSs to sulfur.[30] After the initial activation scan, no obvious change occurs for the subsequent cycles in terms of peak position and intensity, indicating the reversible redox reactions and cycling stability of POAC-4 based Li–S cell (1.0 wt%). All curves of the PVDF and physical mixture based Li–S cells show typical CV characteristics of the sulfur cathodes (Figure S27). Furthermore, the reduction and oxidation peaks of the POAC-4 based Li–S cell (1.0 wt%) appear much sharper than comparisons and the voltage difference (ΔE) between oxidation and reduction peaks is also smaller (Figure S28). Both of the sharper peaks and lower ΔE demonstrate the excellent kinetic performance of the POAC-4 based Li–S cell (1.0 wt%). Figure 4b shows the typical galvanostatic charge-discharge profiles of POAC-4 based Li–S cell (1.0 wt%) within the voltage of 1.7–2.6 V for different cycles at 0.5 C. Two distinct discharge and one charge plateaus have been clearly shown for all profiles, aligning well with the CV observations.

The POAC-4 based Li–S cell (1.0 wt%) delivers an initial specific capacity of 1292.5 mAh g^{-1} at 0.5 C with the CE of 94.5% (Figure 4c). Moreover, a reversible discharge capacity of 805.5 mAh g^{-1} and CE of about 100.0% is obtained after 300 cycles at 0.5 C. By comparison, the physical mixture and PVDF based Li–S cells present discharge specific capacity of 420.8 (CE, 99.8%) and 395.3 (CE, 99.7%) mAh g^{-1} after 300 cycles at 0.5 C, respectively. The superiority of POAC-4 might be attributed to the reason that when it serves as the binder additives can not only help to maintain electrode structure, but also provide a large number of active and catalytic sites, which would contribute to the uniform contact with the conductive skeleton to enhance discharge efficiency and active material utilization, as well accelerate the dissolution of sulfur to promote deep discharge. In comparison, the contrast sample like the physical mixture with separated PVDF and OH-AAn-COF would lack in compatibility with a major part of the binder, thus resulting in unsatisfactory electrochemical performance compared with that of POAC-4. Besides, the cycling performance of POAC-4 based Li–S cell (1.0 wt%) is also much higher than cells with other POAC-4 loadings (i.e. 0.5 wt%, 622.3 mAh g^{-1}; 2.0 wt%, 510.9 mAh g^{-1}; 3.0 wt%, 470.2 mAh g^{-1} and 4.0 wt%, 613.2 mAh g^{-1}) after 300 cycles at 0.5 C (Figure S29). Besides, the cycling performance of POAC-x ($x = 1, 2, 3, 5$) based Li–S cells with 1.0 wt% loading maintain 510.4, 640.1, 647.5 and 431.6 mAh g^{-1} at 0.5 C after 300 cycles, respectively, which show poorer cycling stability than that of POAC-4 based Li–S cell (1.0 wt%) (Figure S30). Notably, the POAC-4 based Li–S cell (1.0 wt%) exhibits superior performance to the most of reported Li–S batteries that applying COFs as the host materials of sulfur (Table S3). Besides, the performance is also higher than reported various binders (e.g., PVP, PVP: PEI, CMC, SBR/CMC and PSF-Im etc.) based Li–S systems, suggesting the superiority of this strategy in enhancing the Li–S battery performance (Table S4). In addition, the Nyquist plots have been evaluated for the cells after 300 cycles and two semicircles in high to medium frequency regions are observed (Figure S31). The resistance of POAC-4 based Li–S cell (1.0 wt%) is much lower than PVDF based Li–S cell after 300 cycles, possibly attributed to the immobilizing and catalytic conversion ability of POAC-4 for LiPSs that enhances the utilization of sulfur and inhibits volume change. Furthermore, the rate capabilities of Li–S cells are investigated at various rates ranging from 0.1 to 2 C, and back to 0.2 C (Figure 4d). POAC-4 based Li–S cell (1.0 wt%) presents

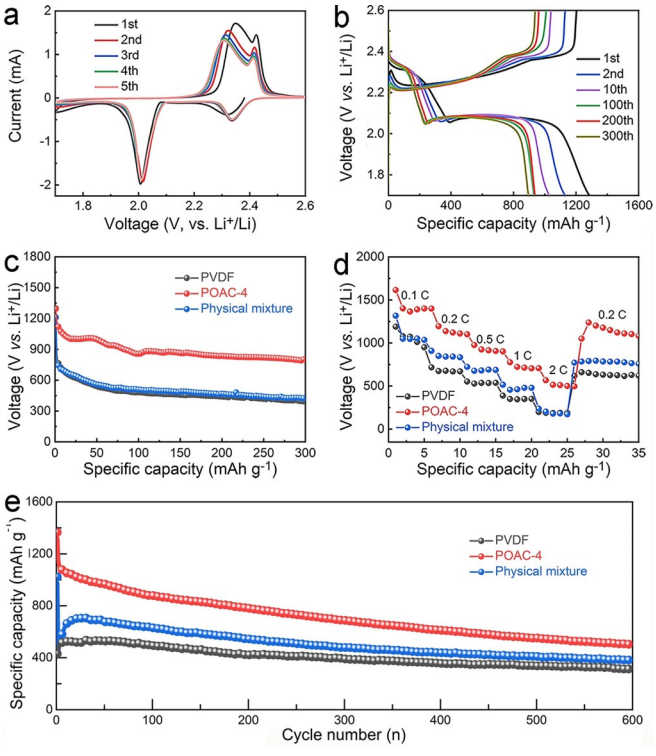

Figure 4. Electrochemical performances of cells based on POAC-4, PVDF and a physical mixture. a) CV curves of a POAC-4 based Li–S cell (1.0 wt%) at a scanning rate of 0.1 mV s^{-1} in the voltage range of 1.7–2.6 V. b) Discharge–charge curves of a POAC-4 based Li–S cell (1.0 wt%) at 0.5 C. c) Cycling performance of cells based on POAC-4, PVDF and a physical mixture at 0.5 C. d) Rate performance of cells based on POAC-4, PVDF and a physical mixture. e) Cycling performance of cells based on POAC-4, PVDF and a physical mixture at 2 C.

the most outstanding rate capability of 1441.6, 1133.3, 925.2, 724.7 and 515.7 mAh g^{-1} at 0.1, 0.2, 0.5, 1 and 2 C, respectively. The capacity is also superior to physical mixture (i.e. 1100.2, 855.2, 691.5, 478.2 and 194.3 mAh g^{-1} at 0.1 C, 0.2, 0.5, 1 and 2 C, respectively) and PVDF (i.e. 1060.6, 681.2, 537.4, 356.9 and 189.8 mAh g^{-1} at 0.1 C, 0.2, 0.5, 1 and 2 C, respectively) based cells. In addition, when the current density is directly decreased back to 0.2 C, its capacity retains as high as 1083.5 mAh g^{-1}, indicating superior high-rate ability. Long-term cycling stability tests of Li–S cells are performed at 2 C (Figure 4e). The retained discharge capacity of POAC-4 based Li–S cell (1.0 wt %) is still maintained at 501.3 mAh g^{-1} after 600 cycles (average CE, ~99.8 %), higher than PVDF (327.7 mAh g^{-1}; average CE, ≈99.4 %) and physical mixture (381.1 mAh g^{-1}; average CE, ≈99.7 %) based Li–S cells. The above results prove the vital role of POAC-4 in the improvement of cell performance.

In order to illustrate the general applicability of micro-additives to improve the electrochemical performance, we have extended the binder system from PVDF to sodium carboxymethylcellulose (CMC) and sodium alginate (SA) (Figures S32 and S33). All the comparison samples are assembled in the same way of POAC-4 based Li–S cell (1.0 wt %) to evaluate the electrochemical performances (detail see Methods). The discharge capacities of CMC@OH-AAn-COF-4 (COAC-4) and SA@OH-AAn-COF-4 (SOAC-4) based Li–S cells obtain 780.4 mAh g^{-1} and 631.6 mAh g^{-1} after 150 cycles at 0.5 C, respectively, higher than bare cells (Figures S34 and S35). To verify the superiority of OH-AAn-COF, other COFs types like DAA-COF[31] and AAn-COF[18b] have been selected as contrast samples to evaluate their battery performances. AAn-COF, iso-reticular to OH-AAn-COF with the only difference of absence of hydroxyl groups in OH-AAn ligand, has been assembled into PVDF@AAn-COF-4 (PAAC-4) (Figures S36 and S37). In addition, DAA-COF, another COF synthesized from TP and anthracene-2,6-diamine (DAA), in which DAA is applied to replace OH-AAn to investigate the vital role of anthraquinone group, has also been prepared as PVDF@DAA-COF-4 (PDAC-4) (Figures S36 and S38). The discharge capacity of PAAC-4 and PDAC-4 based Li–S cells present 631.8 mAh g^{-1} (after 150 cycles) and 608.5 mAh g^{-1} (after 200 cycles) at 0.5 C, which are higher than PVDF based Li–S cell yet are still lower than POAC-4 based one (Figures S39 and S40). These results could prove the vital role of OH-AAn-COF with numerous functional groups like hydroxyl and anthraquinone groups in enhancing the Li–S performance.

In addition, the electrode morphologies have been characterized before and after the 300 cycles by SEM and EDS mapping tests. As shown in Figure S41a and d, the assembled electrode with the POAC-4 as the binder micro-additive is dense with a flat surface without obvious cracks, suggesting the tight contact of sulfur, binder and the conductive additives in the electrode during the cycling. In contrast, the cathode for PVDF based Li–S cell delivers serious aggregation morphology of active material with many cracks after 300 cycles, which is attributed to the rigidity of PVDF that cannot buffer the volume change of the electrode during the cycling (Figure S41c,f). The corresponding SEM and EDS elemental mappings of POAC-4, PVDF, and physical mixture based electrodes after 300 cycles are shown in Figure S42. Sulfur is evenly distributed in the cathode of POAC-4 based Li–S cell (1.0 wt %), indicating the addition of POAC-4 benefits to constructing a stable 3D network, helps to provide superior adherence to stabilize the electrode structure, and catalyzes the decomposition of LiPSs in time. The morphologies of cycled Li anodes that have been matched with POAC-4 and PVDF-based cathodes have also been studied (Figure S43). While the SEM images of the two Li anodes are similar, a much larger amount of sulfur has been detected in the anode of PVDF-based Li–S cell by EDS mapping tests, which confirms that POAC-4 is more beneficial to inhibit the shuttling effect in Li–S cells.

Furthermore, operando Raman spectroscopy is employed to conduct real-time monitoring over the conversion of soluble Li_2S_x upon charging and discharging. Figure 5a,b depict the in situ Raman spectra collected during the electrochemical process. It is noted that the intensities of S_8^{2-} and S_6^{2-} peaks gradually decline and nearly vanish at the end of discharge, followed by regeneration upon charging, corroborating solidly the good reversibility of electrochemical reactions and efficient management of polysulfides within

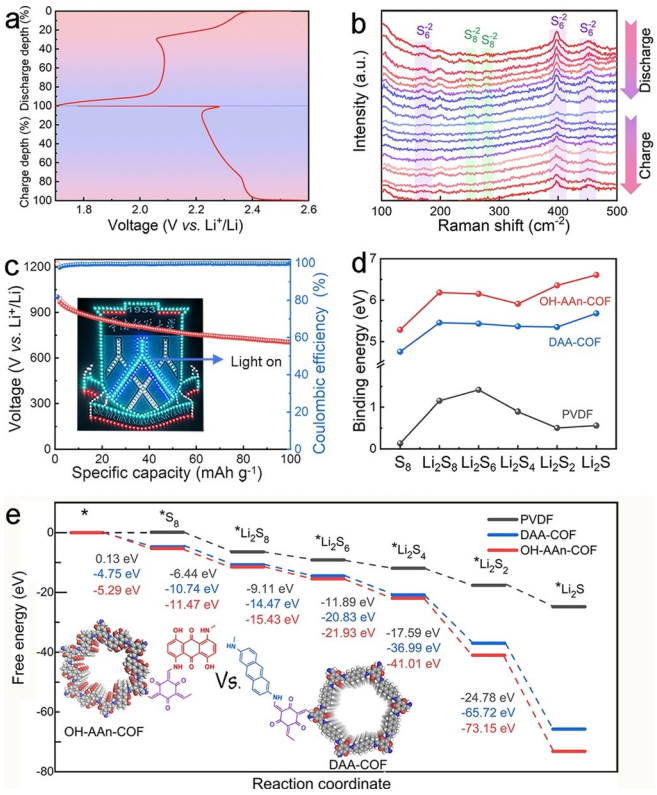

Figure 5. Electrochemical performance and DFT calculations of a POAC-4 based Li–S cell (1.0 wt %). a, b) In situ Raman spectra of a POAC-4 based Li–S cell (1.0 wt %) for real-time monitoring of the conversion of soluble Li_2S_x upon charging and discharging. c) Cycling performance of a POAC-4 based Li–S cell (1.0 wt %) with sulfur loading of 4.0 mg cm^{-2} at 0.5 C. d) The adsorption energy of Li_2S_x on PVDF, DAA-COF and OH-AAn-COF. e) Energy profiles for the reduction of LiPSs on DAA-COF and OH-AAn-COF.

the POAC-4/S || Li cell. Besides, the POAC-4 based Li–S cell (1.0 wt%) harvests a high specific capacity and excellent cycling stability at the sulfur loading of 4 mg cm^{-2} (Figure 5c). At 0.5 C, the POAC-4 based Li–S cell (1.0 wt%) delivers a high initial discharge capacity of 1000.5 mAh g^{-1}, and still maintains at 700.0 mAh g^{-1} after 100 cycles. In contrast, the discharge capacity only maintains 410.2 mAh g^{-1} and 279.3 mAh g^{-1} after 100 cycles for the physical mixture and PVDF based Li–S cells, respectively, which are lower than that of the POAC-4 based Li–S cell (1.0 wt%) (Figure S44). The above results confirm the superiority of POAC-4 to physical mixture and PVDF in maintaining the cycling stability. As a proof-of-concept, the as-assembled POAC-4 based Li–S cell (1.0 wt%) can light up a light-emitting-diode (LED) panel (Figure 5c, inset).

To reveal the possible mechanism, the DFT calculations of the adsorption and catalytic conversion effects of LiPSs on PVDF, DAA-COF and OH-AAn-COF have been studied. The binding energy, Eb, is computed to measure the binding strength of Li_2S_x on these substrates to evaluate the adsorption ability. The binding energy is defined as $E_{(absorb)} = E_{(Substrate\ +\ Li2Sx)} - E_{(Substrate)} - E_{(Li2Sx)}$, and the more positive or larger value means the stronger anchoring effect of Li_2S_x on the substrates. On the basis of the calculation results, the binding energy of Li_2S_8, Li_2S_6, Li_2S_4, Li_2S_2, and Li_2S on OH-AAn-COF are 6.18, 6.15, 5.91, 6.36, and 6.61 eV, respectively (Figure 5d and Figure S45). Notably, DFT results show that OH-AAn-COF has the strongest adsorption ability for LiPSs compared with PVDF and DAA-COF. Specially, OH-AAn-COF possesses the highest binding energy of 6.61 eV with Li_2S owing to the direct bonding effect between the S atoms of Li_2S and OH-AAn-COF (Figure 5d). It is noted that the more negative of the binding energy, the stronger suppression for the shuttling effect.[30] This indicates that OH-AAn-COF exhibits the best potential on mitigating LiPSs dissolution and suppressing shuttling effect in Li–S batteries and are consistent with the above-mentioned experimental results, which suggests that the $S_8 \rightleftharpoons Li_2S$ reaction can be tuned by OH-AAn-COF.[29b,30,32]

In addition, we have proved that COFs as microadditives can possess catalytic activity in experiment results. To this end, the overall reactions based on the reversible formation of Li_2S from S_8 and Li bulk are calculated based on the DFT calculations (the asterisk stands for the adsorption site, and the detailed reaction equations are shown in Table S5). Figure 5e shows the calculated Gibbs free energy of S-containing disproportionation products including S_8, Li_2S_8, Li_2S_6, Li_2S_4, Li_2S_2 and Li_2S in the conversion reaction for OH-AAn-COF, DAA-COF and PVDF (Figure 5e).[25a,29a,30] From the free energy graph of reaction, we can clearly see that the Gibbs free energy of OH-AAn-COF is much lower than the two comparative samples (DAA-COF and PVDF), among which the Gibbs free energy of DAA-COF is also lower than pure PVDF. This corresponds to the experimental results that OH-AAn-COF is favorable for product formation. In these reactions of $S_8 \rightleftharpoons Li_2S$, the Gibbs free energy gradually becomes more negative, which indicates the reaction is spontaneous at room temperature. Moreover, it shows that OH-AAn-COF plays a significant role in promoting the catalytic conversion of LiPSs compared with DAA-COF and PVDF. At the same time, we find that the anthraquinone group in OH-AAn-COF is more effective than the anthracene group in DAA-COF during the catalytic conversion process, which also complies with the battery performance that OH-AAn-COF is superior to DAA-COF (Figure S46). By comparison, the Gibbs free energy of ordinary keto-carbonyl groups for OH-AAn-COF and DAA-COF is not obvious (Figure S47).[25a] In addition, the reaction of $Li_2S_6 \rightarrow Li_2S_4$ has the highest positive Gibbs free energy, indicating that this is the rate-limiting step of Li–S batteries (Figure S46). Above all, the DFT calculations have proven the vital role of anthraquinone COFs in immobilizing and catalytically converting LiPSs. Fast nucleation/conversion of the LiPSs is realized in an ideal manner at the interface; as a result, the LiPSs shuttling is effectively restrained, thus improving the Li–S battery performances. Therefore, characterizations like in situ Raman spectroscopy, *ex situ* XPS, UV/Vis, rheological behavior, SEM, and electrochemical investigations combined with DFT calculations has properly supported the vital role of POAC-*x* (1–5) as the microadditives of binder in enhancing the Li–S battery performance.

Conclusion

In summary, we have established that COFs could have implications as microadditives of binders ($\approx$1.0 wt% in cathode) and a series of anthraquinone COF-based hollow tubes have been prepared as model microadditives. The microadditives can strengthen the basic properties of the binder and effectively immobilize and catalytically convert LiPSs as proved by the DFT results. Thus-obtained anthraquinone COF-based hollow tubes can serve as microadditives and present extraordinary performance. Specifically, electrodes with the as-prepared POAC-4 as microadditive (1.0 wt% in the cathode) can present the highest reversible capacity of 805.5 mAh g^{-1} after 300 cycles at 0.5 C with the CE of $\approx$99.9%, almost doubly enhanced than that of the bare electrode. Notably, the achieved performances are superior to most reported COF-based or binder-based Li–S batteries. This study paves a new avenue to develop COFs as microadditives of binders for high-performance Li–S batteries and energy applications, which might expedite the investigation of COFs in this field.

Acknowledgements

This work was financially supported by NSFC (No. 22171139, 21871141, 21871142, 21901122 and 92061101); the Natural Science Research of Jiangsu Higher Education Institutions of China (19KJB150011) and Project funded by China Postdoctoral Science Foundation (No. 2018M630572 and 2019M651873); Priority Academic Program Development of Jiangsu Higher Education Institutions and the Foundation of Jiangsu Collaborative Innovation Center of Biomedical Functional Materials.

Conflict of Interest

The authors declare no conflict of interest.

Keywords: anthraquinone · batteries · covalent organic frameworks · Li–S batteries · microadditives

[1] a) X. Ji, K. T. Lee, L. F. Nazar, *Nat. Mater.* **2009**, *8*, 500–506; b) S. Bai, X. Liu, K. Zhu, S. Wu, H. Zhou, *Nat. Energy* **2016**, *1*, 16094; c) C. Zhao, G. Xu, Y. Zhou, L. Zhang, I. Hwang, Y.-X. Mo, Y. Ren, L. Cheng, C.-J. Sun, Y. Ren, X. Zuo, J.-T. Li, S.-G. Sun, K. Amine, T. Zhao, *Nat. Nanotechnol.* **2021**, *16*, 166–173.

[2] a) M. Jana, R. Xu, X.-B. Cheng, J. S. Yeon, J. M. Park, J.-Q. Huang, Q. Zhang, H. S. Park, *Energy Environ. Sci.* **2020**, *13*, 1049–1075; b) Q. Pang, X. Liang, C. Y. Kwok, L. F. Nazar, *Nat. Energy* **2016**, *1*, 16132.

[3] a) R. Li, D. Rao, J. Zhou, G. Wu, G. Wang, Z. Zhu, X. Han, R. Sun, H. Li, C. Wang, W. Yan, X. Zheng, P. Cui, Y. Wu, G. Wang, X. Hong, *Nat. Commun.* **2021**, *12*, 3102; b) J. Qian, Y. Xing, Y. Yang, Y. Li, K. Yu, W. Li, T. Zhao, Y. Ye, L. Li, F. Wu, R. Chen, *Adv. Mater.* **2021**, 2100810; c) F. Liu, G. Sun, H. B. Wu, G. Chen, D. Xu, R. Mo, L. Shen, X. Li, S. Ma, R. Tao, X. Li, X. Tan, B. Xu, G. Wang, B. S. Dunn, P. Sautet, Y. Lu, *Nat. Commun.* **2020**, *11*, 5215.

[4] P. Chen, Z. Wu, T. Guo, Y. Zhou, M. Liu, X. Xia, J. Sun, L. Lu, X. Ouyang, X. Wang, Y. Fu, J. Zhu, *Adv. Mater.* **2021**, *33*, 2007549.

[5] a) H. Chen, M. Ling, L. Hencz, H. Y. Ling, G. Li, Z. Lin, G. Liu, S. Zhang, *Chem. Rev.* **2018**, *118*, 8936–8982; b) W. Chen, T. Lei, T. Qian, W. Lv, W. He, C. Wu, X. Liu, J. Liu, B. Chen, C. Yan, J. Xiong, *Adv. Energy Mater.* **2018**, *8*, 1702889.

[6] a) Q. Guo, Z. Zheng, *Adv. Funct. Mater.* **2020**, *30*, 1907931; b) S. L. Chou, Y. Pan, J. Z. Wang, H. K. Liu, S. X. Dou, *Phys. Chem. Chem. Phys.* **2014**, *16*, 20347–20359.

[7] a) H. Yuan, J.-Q. Huang, H.-J. Peng, M.-M. Titirici, R. Xiang, R. Chen, Q. Liu, Q. Zhang, *Adv. Energy Mater.* **2018**, *8*, 1802107; b) S. Choi, T. W. Kwon, A. Coskun, J. W. Choi, *Science* **2017**, *357*, 279–283; c) C. Wang, H. Wu, Z. Chen, M. T. McDowell, Y. Cui, Z. Bao, *Nat. Chem.* **2013**, *5*, 1042–1048.

[8] F. Zou, A. Manthiram, *Adv. Energy Mater.* **2020**, *10*, 2002508.

[9] a) H. W. Chen, C. Wang, Y. Dai, J. Ge, W. Lu, J. Yang, L. Chen, *Nano Energy* **2016**, *26*, 43–46; b) W. Chen, T. Qian, J. Xiong, N. Xu, X. Liu, J. Liu, J. Zhou, X. Shen, T. Yang, Y. Chen, C. Yan, *Adv. Mater.* **2017**, *29*, 1605160.

[10] a) A. P. Côté, A. I. Benin, N. W. Ockwig, M. O'Keeffe, A. J. Matzger, O. M. Yaghi, *Science* **2015**, *310*, 1166–1170; b) Y. Li, W. Chen, G. Xing, D. Jiang, L. Chen, *Chem. Soc. Rev.* **2020**, *49*, 2852–2868; c) K. Geng, T. He, R. Liu, S. Dalapati, K. T. Tan, Z. Li, S. Tao, Y. Gong, Q. Jiang, D. Jiang, *Chem. Rev.* **2020**, *120*, 8814–8933.

[11] a) L. Zhou, S. Jo, M. Park, L. Fang, K. Zhang, Y. Fan, Z. Hao, Y.-M. Kang, *Adv. Energy Mater.* **2021**, *11*, 2003054; b) Z. Zheng, H. Ye, Z. Guo, *Energy Environ. Sci.* **2021**, *14*, 1835–1853; c) X. Hu, L. Zhong, C. Shu, Z. Fang, M. Yang, J. Li, D. Yu, *J. Am. Chem. Soc.* **2020**, *142*, 4621–4630; d) E. Vitaku, C. N. Gannett, K. L. Carpenter, L. X. Shen, H. D. Abruna, W. R. Dichtel, *J. Am. Chem. Soc.* **2020**, *142*, 16–20.

[12] a) Z. A. Ghazi, L. Zhu, H. Wang, A. Naeem, A. M. Khattak, B. Liang, N. A. Khan, Z. Wei, L. Li, Z. Tang, *Adv. Energy Mater.* **2016**, *6*, 1601250; b) B. Y. Lu, Z. Q. Wang, F. Z. Cui, J. Y. Li, X. H. Han, Q. Y. Qi, D. L. Ma, G. F. Jiang, X. X. Zeng, X. Zhao, *ACS Appl. Mater. Interfaces* **2020**, *12*, 34990–34998; c) Z. Yang, C. Peng, R. Meng, L. Zu, Y. Feng, B. Chen, Y. Mi, C. Zhang, J. Yang, *ACS Cent. Sci.* **2019**, *5*, 1876–1883; d) X. D. Chen, Y. J. Xu, F. H. Du, Y. Wang, *Small Methods* **2019**, *3*, 1900338.

[13] a) Y. M. Acevedo, N. Sengar, M. Min, P. Clancy, *ACS Appl. Mater. Interfaces* **2020**, *12*, 48957–48968; b) S. Y. Ding, J. Gao, Q. Wang, Y. Zhang, W. G. Song, C. Y. Su, W. Wang, *J. Am. Chem. Soc.* **2011**, *133*, 19816–19822; c) H. Li, J. Ding, X. Guan, F. Chen, C. Li, L. Zhu, M. Xue, D. Yuan, V. Valtchev, Y. Yan, S. Qiu, Q. Fang, *J. Am. Chem. Soc.* **2020**, *142*, 13334–13338.

[14] T. Sun, J. Xie, W. Guo, D. S. Li, Q. Zhang, *Adv. Energy Mater.* 2**020**, 10, 1904199.

[15] S. H. Je, H. J. Kim, J. Kim, J. W. Choi, A. Coskun, *Adv. Funct. Mater.* **2017**, *27*, 1703947.

[16] Q. Qi, X. H. Lv, W. Lv, Q.-H. Yang, *J. Energy Chem.* **2019**, *39*, 88–100.

[17] B. Li, S. Zhang, L. Kong, H. Peng, Q. Zhang, *Adv. Mater.* **2018**, *30*, 1707483.

[18] a) B. Dong, W. Wang, W. Pan, G. J. Kang, *Mater. Chem. Phys.* **2019**, *226*, 244–249; b) M. Liu, Y.-R. Wang, H.-M. Ding, M. Lu, G.-K. Gao, L.-Z. Dong, Y. Chen, S.-L. Li, Y.-Q. Lan, *Sci. Bull.* **2021**, *66*, 1659–1668.

[19] a) S. Mukherjee, M. Das, A. Manna, R. Krishna, S. Das, *Chem. Mater.* **2019**, *31*, 3929–3940; b) G. Chen, X. Wang, J. Li, W. Hou, Y. Zhou, J. Wang, *ACS Appl. Mater. Interfaces* **2015**, *7*, 18508–18518.

[20] T. H. Zhou, Y. Zhao, J. W. Choi, A. Coskun, *Angew. Chem. Int. Ed.* **2019**, *58*, 16795–16799; *Angew. Chem.* **2019**, *131*, 16951–16955.

[21] S. Liu, J. Li, X. Shi, E. Gao, Z. Xu, H. Tang, K. Tong, Q. Pei, J. Liang, Y. Chen, *Adv. Electron. Mater.* **2017**, *3*, 1700098.

[22] J. Liang, L. Li, K. Tong, Z. Ren, W. Hu, X. Niu, Y. Chen, Q. Pei, *ACS Nano* **2014**, *8*, 1590–1600.

[23] E. C. Garnett, W. Cai, J. J. Cha, F. Mahmood, S. T. Connor, M. Greyson Christoforo, Y. Cui, M. D. McGehee, M. L. Brongersma, *Nat. Mater.* **2012**, *11*, 241–249.

[24] J. Ge, H.-B. Yao, X. Wang, Y.-D. Ye, J.-L. Wang, Z.-Y. Wu, J.-W. Liu, F.-J. Fan, H.-L. Gao, C.-L. Zhang, S.-H. Yu, *Angew. Chem. Int. Ed.* **2013**, *52*, 1654–1659; *Angew. Chem.* **2013**, *125*, 1698–1703.

[25] a) Q. Qi, Y. Deng, S. Gu, M. Gao, J.-Y. Hasegawa, G. Zhou, X. Lv, W. Lv, Q.-H. Yang, *ACS Appl. Mater. Interfaces* **2019**, *11*, 47956–47962; b) Y. Yao, H. Wang, H. Yang, S. Zeng, R. Xu, F. Liu, P. Shi, Y. Feng, K. Wang, W. Yang, X. Wu, W. Luo, Y. Yu, *Adv. Mater.* **2020**, *32*, 1905658.

[26] L. L. Kong, L. Wang, Z. C. Ni, S. Liu, G. R. Li, X. P. Gao, *Adv. Funct. Mater.* **2019**, *29*, 1808756.

[27] Y. Xie, G. Pan, Q. Jin, X. Qi, T. Wang, W. Li, H. Xu, Y. Zheng, S. Li, L. Qie, Y. Huang, J. Li, *Adv. Sci.* **2020**, *7*, 1903168.

[28] H. Shi, X. Ren, J. Lu, C. Dong, J. Liu, Q. Yang, J. Chen, Z.-S. Wu, *Adv. Energy Mater.* **2020**, *10*, 2002271.

[29] a) G. Zhou, S. Zhao, T. Wang, S. Z. Yang, B. Johannessen, H. Chen, C. Liu, Y. Ye, Y. Wu, Y. Peng, C. Liu, S. P. Jiang, Q. Zhang, Y. Cui, *Nano Lett.* **2020**, *20*, 1252–1261; b) C.-Y. Chen, H.-J. Peng, T.-Z. Hou, P.-Y. Zhai, B.-Q. Li, C. Tang, W. Zhu, J.-Q. Huang, Q. Zhang, *Adv. Mater.* **2017**, *29*, 1606802.

[30] G. Li, X. Wang, M. H. Seo, M. Li, L. Ma, Y. Yuan, T. Wu, A. Yu, S. Wang, J. Lu, Z. Chen, *Nat. Commun.* **2018**, *9*, 705.

[31] X. Li, J. Qiao, S. Chee, H. Xu, X. Zhao, H. S. Choi, W. Yu, S. Y. Quek, U. Mirsaidov, K. Loh, *J. Am. Chem. Soc.* **2020**, *142*, 4932–4943.

[32] a) H. K. Zhang, Z. L. Wang, J. H. Ren, J. Y. Liu, J. J. Li, *Energy Storage Mater.* **2021**, *35*, 88–98; b) Y. Tsao, M. Lee, E. C. Miller, G. Gao, J. Park, S. Chen, T. Katsumata, H. Tran, L.-W. Wang, M. F. Toney, Y. Cui, Z. Bao, *Joule* **2019**, *3*, 872–884.

Manuscript received: October 1, 2021
Accepted manuscript online: October 29, 2021
Version of record online: December 3, 2021